# Localized surface plasmon resonance biosensor: an improved technique for SERS response intensification

**Md. Saiful Islam,**[1,2,*] **Jakeya Sultana,**[1] **Rifat Ahmmed Aoni,**[3] **Md. Selim Habib,**[4]
**Alex Dinovitser,**[1] **Brian W.-H. Ng,**[1] **and Derek Abbott**[1]

[1]*School of Electrical & Electronic Engineering, University of Adelaide, Adelaide, SA 5005, Australia*
[2]*Institute of Photonics & Advance Sensing (IPAS), University of Adelaide, Adelaide, SA 5005, Australia*
[3]*Nonlinear Physics Centre, Research School of Physics and Engineering, Australian National University, Canberra, Acton, ACT 2601, Australia*
[4]*College of Optics and Photonics, University of Central Florida, Orlando, Florida 32816, USA*
*\*Corresponding author: mdsaiful.islam@adelaide.edu.au*

As technology continues to advance, the development of novel sensing systems opens new possibilities for low-cost, practical biosensing applications. In this Letter, we demonstrate a localized surface plasmon resonance system that combines both wave-guiding and plasmonic resonance sensing with a single microstructured polymeric structure. Characterizing the sensor using the finite element method simulation shows, to the best of our knowledge, a record wavelength sensitivity (WS) of 111000 nm/refractive index unit (RIU), high amplitude sensitivity (AS) of 2050 RIU$^{-1}$, high sensor resolution and limit of detection of $9 \times 10^{-7}$ RIU and $8.12 \times 10^{-12}$ RIU$^2$/nm, respectively. Furthermore, these sensors have the capability to detect an analyte within the refractive index range of 1.33–1.43 in the visible to mid-IR, therefore being potentially suitable for applications in biomolecular and chemical analyte detection. © 2019 Optical Society of America

https://doi.org/10.1364/OL.44.001134

Localized surface plasmon resonance (LSPR) is an optical phenomenon that is a result of surface plasmon excitation in nanoparticles or nanogratings of a size smaller than the wavelength of light. The high optical confinement and local field enhancement capability of LSPR are widely implemented for surface-enhanced Raman scattering (SERS) analysis, where enhanced electromagnetic (EM) fields near metal nanostructure promote a significant Raman response of deposited proteins/molecules that are in contact with the metal [1] . The use of photonic crystal fiber (PCF) has advantages in terms of tunability, size, and immunity to electromagnetic interference in combination with LSPR makes the sensor suitable for a range of sensing applications. For bioanalyte detection and SERS response intensification, several studies with different techniques, including surface plasmon resonance (SPR) and LSPR have been carried

out [2–5] . Using tungsten disulfide to support SPR, a sensitivity of 2459.3 nm/RIU for a refractive index (RI) ranging from 1.33 to 1.36 has been reported [2] . Using a D-shaped fiber structure, researchers obtained a maximum WS of 44567 nm/RIU [3] . Note that recent studies [2–5] were carried out using SPR technology, and used either internal or external sensing with a D-shaped structure. In internal sensing, the filling and flushing of the analyte are challenging, whereas the D-shaped PCF requires external surface polishing to give its shape. Here internal sensing refers to filling various air holes with the analyte solution—this can be carried out via a syringe (i.e., withdrawal or pumping mode)—whereas external sensing refers to contacting the analyte to the fiber surface. Note that our recent study on SPR showed a high WS (62,000 nm/RIU) and AS (1415 RIU$^{-1}$) that comes with a high confinement loss (CL) (300 dB/cm) [6] . However, it has been necessary to eliminate thick cladding layers from these fibers to allow fields to interact directly through evanescent waves arising from the core/cladding boundary region, resulting in a loss of mechanical strength. Therefore, LSPR-based sensors are introduced as a solution to enhance the sensing performance as well as minimizing the size and cost [5,7] . Using nanospheres, researchers were able to achieve a maximum WS of 27,000 nm/RIU [7] whereas the use of a Au grating reports a maximum WS of 3340 nm/RIU with extremely low AS that also comes with a high CL [5] . Therefore, there is scope to develop an improved theoretical framework of PCF-based biosensors that may eventually lead to different practical implementations in both the medical and chemical industries.

In this Letter, we aim to design a sensor that can improve the absorption, resolution, and limit of detection (LOD) with a low CL. Therefore, we propose a LSPR sensor having an Au grating as a plasmonic metal with the analyte channel in contact with Au that facilitates external sensing. Considering the fabrication feasibility, we describe the optimized sensor

by analyzing different structures with variations in key geometrical parameters.

The design [Fig. 1(a)] and computational analysis of the sensor are carried out using COMSOL multiphysics 5.3 set to an extremely fine mesh size with a degree of freedom of 7,39,945, number of elements of 1,05,616, and minimum element quality of 0.324. On a silica ($SiO_2$) substrate, the air holes are placed so as to confine the electric field to the center of the fiber and interact strongly with the metal. A thinner $TiO_2$ layer is used in contact with the $SiO_2$ so that the Au can adhere strongly. The basic data for the model, such as the RI of $SiO_2$, $TiO_2$, and Au are obtained from Refs. [8–10]. The air hole diameters, radius, and pitch of the PCF are defined as $d_1$, $d_2$, $d_3$, $r_1$, and $\Lambda_1$, respectively; and $TiO_2$, Au, analyte, and the perfectly matched layer (PML) are defined as $t_t$, $t_g$, $t_a$, and $t_p$, respectively. Note that the PML is a computational boundary that absorbs scattered waves from the PCF. The scaled down air holes $d_2$ and $d_3$ help to reduce the CL, as it contributes to the reduced scattering of light from the center of the fiber. The stacked capillary diagram of the sensor is shown in Fig. 1(b) showing that it can be fabricated using capillary stacking. In terms of fabrication, the thicker wall capillary indicates smaller air holes, and the solid rods indicate no air holes. Figure 1(c) indicates that when the phase matching of $Re(n_{eff})$ between the core guided mode and SPP mode occurs then the sensor is then at resonance and, thus, a maximum loss peak is obtained. The inset of Fig. 1(c) shows the electric field distribution in the core guided mode (i) and the SPP mode (ii).

We considered $d_c = 0.18\Lambda$, $d = 0.70\Lambda$, $d_1 = 0.09\Lambda$, $\Lambda = 3.75$ μm, $t_a = 1.5$ μm, and $t_p = 1.80$ μm and varied the Au and $TiO_2$ thickness, respectively, to get the optimum $t_g$ and $t_t$; then at the optimum $t_g$ and $t_t$ we characterize the sensor with SPR and LSPR. Starting with Au, we vary the $t_g$ to 20 nm, 30 nm, and 40 nm and the obtained characteristics that are shown in Figs. 2(a) and 2(b). Comparing 20 nm and 30 nm, we can see that the obtained CL for 20 nm is less than 30 nm. Though the AS is almost the same, the WS for 30 nm is higher (15000 nm/RIU) than 20 nm (8000 nm/RIU). Therefore, we choose 30 nm as the optimum. Now, comparing 30 nm with 40 nm, we see that the loss peak broadens at 40 nm; thus, the AS also reduces in a large scale, as shown in Figs. 2(a) and 2(b). Thus, considering the loss, WS, and AS, we consider 30 nm as the optimum Au thickness. Here the CL, WS, and AS are calculated using the equa-
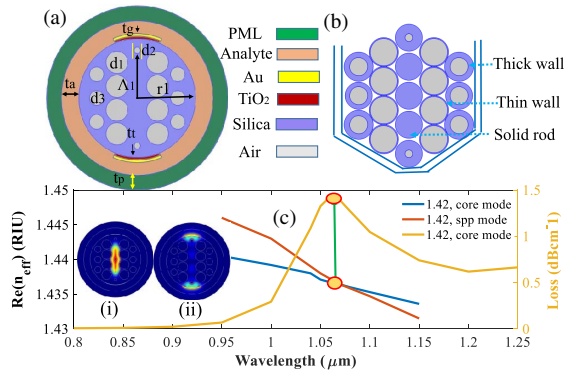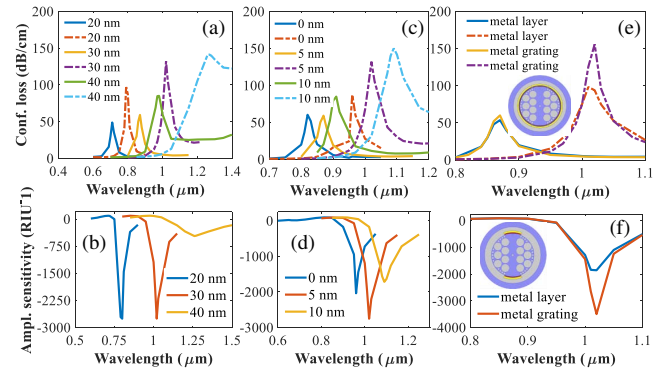


**Fig. 2.** (a), (b) CL and AS with $t_g$ variation; (c), (d) CL and AS with $t_t$ variation; and (e), (f) CL and AS having SPR and LSPR.

tion $8.686 \frac{2\pi}{\lambda} Im(n_{eff}) \times 10^4$ (dB/cm), $\frac{\Delta\lambda_{peak}}{\Delta n_a}$ (nm/RIU), and $-\frac{1}{\alpha(\lambda, n_a)} \frac{\delta\alpha(\lambda, n_a)}{\delta n_a}$ (RIU$^{-1}$) [6] , respectively, where $\Delta\lambda_{peak}$, and $\Delta_{na}$ indicates the peak wavelength difference and change in analyte RI, and the overall loss and the difference between two loss spectra are denoted by $\alpha(\lambda, n_a)$ and $\delta\alpha(\lambda, n_a)$.

The optimization of $TiO_2$ is illustrated in Figs. 2(c) and 2(d). It indicates that without $TiO_2$ the CL is low; however, that comes with low WS and AS because $TiO_2$ has a high RI and acts as a transition metal and, when placed between $SiO_2$ and Au, it generates a large number of electrons at the surface. This creates a strong evanescent wave and attracts the fields from the core to interact strongly with the plasmonic mode and, therefore, increases the CL, which also increases the sensitivity. Without the $TiO_2$ coating, the Au exhibits poor adhesion and easily flakes off with light pressure [11] . To provide proper adhesion, a thin layer of $TiO_2$ is included to provide the necessary adhesion. A 10 nm coating between the $SiO_2$ and the Au, increases the CL and broadens the loss peak. However, a slightly thinner layer (5 nm) is found to restore the sharp loss peak, which is required to achieve the high AS.

The reason for utilizing LSPR instead of SPR is shown in Figs. 2(e) and 2(f). We observe that with LSPR a sharper loss peak results in around 1.85 times larger AS than with SPR. In LSPR, the excitation of surface electrons occurs over a small portion of surface that results in lowering the CL. This is because plasmons are only created in a localized area and not on the whole surface. Note that this is also the reason for obtaining a sharper loss peak, as fields from the core can strongly interact with the specified portion of the surface. The corresponding WS and AS with LSPR and SPR are 14000 nm/RIU, 15000 nm/RIU and 3500 RIU$^{-1}$, 1900 RIU$^{-1}$, respectively. Moreover, LSPR requires less Au and $TiO_2$, which may result in improved cost-effectiveness for real-world applications. Note that, in Figs. 2–4, the solid and dashed lines indicate the performance for an RI of 1.41 and 1.42, respectively.

Considering the LSPR at the optimum Au and $TiO_2$ thickness, we then optimize the analyte and PML. We start with the analyte layer and vary it to 1.2 μm, 1.5 μm, 1.8 μm, and 2.1 μm. The characteristics shown in Figs. 3(a) and 3(b) illustrate that at low $t_a$, the sensor experiences low loss; however, that comes with low AS (1350 RIU$^{-1}$). As $t_a$ increases, the loss peaks begin sharpening, and a sharper loss peak is obtained at $t_a = 1.8$ μm. Therefore, maximum AS (3500 RIU$^{-1}$) is



**Fig. 1.** (a) Schematic of the cross section; (b) stacked preform and (c) dispersion relation of the proposed LSPR sensor.

obtained at that thickness. Increasing from 1.8 μm, we can see that the AS starts to decrease. Therefore, considering the loss peak broadening and AS, we choose 1.8 μm as the optimum $t_a$. Then, keeping $t_a$ fixed to 1.8 μm, we optimize the $t_p$. We can see that at $t_p = 1.50$ μm the AS is low compared to $t_p = 1.80$ μm and 2.1 μm. However, when we increase $t_p$ to 1.80 μm, the AS also increases, and any further increase of PML does not change the characteristics of the fiber sensor. Therefore, we choose 1.80 μm as the optimum PML thickness.

Until now, we have optimized different geometrical parameters, including the selection between SPR and LSPR, by considering few smaller air holes of diameter $d_{c_1} = d_c$, closest to the sensing surface, as shown in Figs. 2(e), 2(f), and 3(e). The reason for utilizing such small air holes is to help confine more light into the core and prevent scattering out to the surface. We can see from Figs. 3(e) and 3(f) that with $d_{c_1}$ near the surface the sensor shows a remarkable AS with a sharper loss peak. However, a number of holes close to the surface create fabrication difficulties. The reason is that there is insufficient space near the surface to place the same sized capillary to produce the smaller air holes. One possible solution may be to use a smaller size capillary outer diameter. However, different sized holes during the fiber drawing process are problematic in terms of maintaining even pressure through all the holes. Considering this fact and, in order to simplify the design, we remove $d_{c_1}$ and characterize the sensor. We find that [Figs. 3(e) and 3(f)] removing $d_{c_1}$ reduces the sensing performance and increases the loss (AS reduces to 2850 RIU$^{-1}$ from 3500 RIU$^{-1}$). However, considering the feasibility of fabrication, we choose the sensor without $d_{c_1}$ as the optimum [as shown in the inset of Fig. 3(f)].

The analysis illustrated in Figs. 2 and 3 shows that the optimized sensor exhibits high CL, which is a limitation in terms of practical implementations of the sensor, because it also limits the sensor length. Note that we place an air hole at the center of diameter $d_c = d_2 = 0.18\Lambda$, so that it can deflect the EM waves from the center towards the metal dielectric interface. The motivation is to enhance the light-matter interaction; however, that comes with a high CL. We find that the removal of $d_c$ decreases the CL significantly whereas the resulting change in WS and AS is almost negligible [Figs. 4(a) and 4(b)]. Therefore, considering the CL, we choose the sensor structure without $d_c$ as optimum.

The fabrication of the fiber shown in Fig. 4(b) is still challenging because position of $d_2$ is so close to the surface. It is impossible to place a capillary of size $d_1$ at the position of $d_2$ and maintain the shape of the surface. Several solutions to these problems have been considered, including (1) removing $d_2$, (2) increasing $r_1$, and (3) reducing $\Lambda_1$, or (4) machining the surface of the silica preform after fabrication. We characterize the sensor considering all the possible solutions, and the obtained characteristics are shown in Figs. 4(c) and 4(d). We started by removing $d_2$ and found that a high AS of 2360 RIU$^{-1}$ can be obtained but with a high CL of 34 dB/cm for 1.41 and 75 dB/cm for 1.42 than with $d_2$. This is because without $d_2$ the EM waves from the center of the fiber interact directly with the metal that assists in creating high sensitivity; however, this comes at the price of large scattering that results in a high CL. Therefore, it is important to limit the scattering of light, and, thus, we decide to retain $d_2$, but with optimized position, so that loss can be reduced further maintaining sensitivity and fabrication feasibility.

Next, keeping $d_2$ in its previous position ($\Lambda_1 = 1.75\Lambda$), we then increased $r_1$ from where we find an extremely low AS of 122 RIU$^{-1}$ with a broadening of the loss peak. Therefore, without varying $r_1$, we place $d_2$ in a position where capillaries of diameter $d_1$ can be used to create both hole sizes required for this design. As such, we reduce $\Lambda_1$ to $1.5\Lambda$ and maintain sufficient space from the surface to the air hole. Fabrication will use pressurization of the capillaries to achieve the desired size of $d_2$. We can see the resulting characteristics [from Figs. 4(c) and 4(d)] with an extremely low CL (3 dB/cm for 1.41 and 8 dB/cm for 1.42). The optimized sensor [shown in Fig. 4(d)] also exhibits a high AS of 2050 RIU$^{-1}$ and WS of 111000 nm/RIU.

However, in the present optimized structure, there is another problem that is still challenging for fabrication. We can see that [as shown in the inset of Fig. 4(d)] the air hole of diameter $d_3$ is still close to the surface that may also be a challenge for fabrication. Note that it is necessary to keep $d_3$ so that it can act as an obstacle for scattered light from the core and assist with tighter confinement at the center of the fiber. Considering the fabrication difficulties there are two possible solutions to facilitate fabrication. One is to increase $r_1$, and the other is to reduce $d_3$ and characterize the sensing performance. Previously, we observed that increasing $r_1$ dramatically reduces the AS and, therefore, the only option now is to reduce $d_3$. Reducing $d_3$ to $2/3d$, we can see that the CL, AS, and WS have not changed notably. The reason is the pitch distance
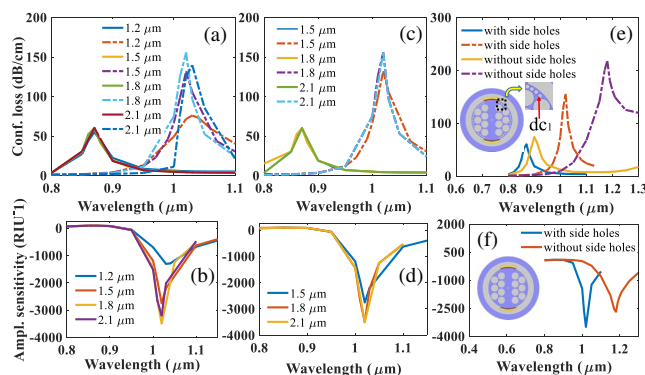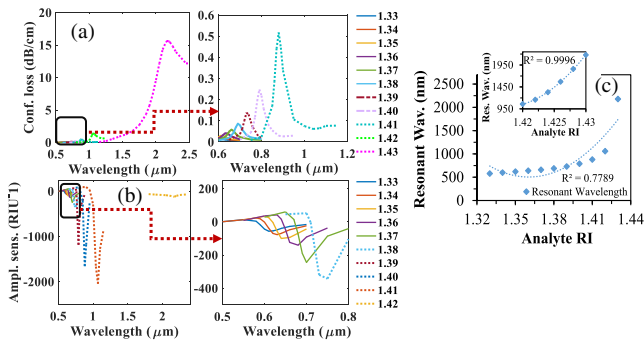


**Fig. 3.** (a), (b) CL and AS having $t_a$ variation; (c), (d) having $t_p$ variation; and (e), (f) having side air holes near the surface.
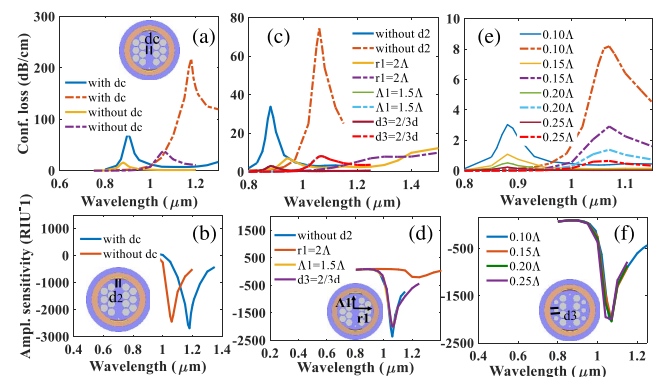


**Fig. 4.** (a), (b) CL and AS of the LSPR sensor with and without $d_c$; (c), (d) having the effect of $d_2$, $r_1$, $\Lambda_1$, and $d_3$; and (e), (f) having different sizes of $d_2$.

**Fig. 5.** (a) CL, (b) AS, and (c) fiber linearity having optimized geometrical parameters of the sensor.

between $d_1$ in the first ring of cladding. Note that the reduced diameter for $d_3$ is still larger than the spacing between $d_1$. Therefore, $d_3$ is able to reflect back the scattered light inside the center of the fiber to maintain the performance with easier fabrication. Thus, we choose $d_3 = 2/3d_1$ as the optimum.

Note that the size of $d_2$ also has impact on the CL and sensitivity; therefore, we also optimize it as shown in Figs. 4(e) and 4(f). We found that increasing size of $d_2$ decreases the CL. However, careful attention should also be given to choose the optimum $d_2$, so that the light waves get a sufficient path to interact with the plasmonic metal at the surface. A larger $d_2$ acts as an obstacle to the interaction of the light from the core with the portion of metal surface. Therefore, after a certain diameter of $d_2$, with the reduction of the CL, the WS and AS also start to reduce and loss peak starts to get broad again. Thus, considering the CL, WS, and AS we choose $d_2 = 0.20\Lambda$ as the optimum.

The CL and sensitivity experienced by the sensor with the changing of the RI is shown in Figs. 5(a) and 5(b). It can be seen that the sensor is highly sensitive with the change of environment RI which also comes with negligible CL. As shown in Fig. 5(a), with an extremely low CL the corresponding resonance wavelengths for RI 1.33 to 1.43 are found at 580, 600, 620, 640, 660, 690, 730, 790, 880, 1060, and 2180 nm respectively. Note that the increment of the CL with RI is due to the lower penetration of the EM field towards the core and higher penetration towards the LSPR region. Therefore, according to the resonance peak shift, we obtain a record WS of 1,11,000 nm/RIU; having a sharp resonance peak, the sensor also attains a record AS of 2050 RIU$^{-1}$. To the best of our knowledge, the obtained WS and AS are the maximum with minimum CL, respectively, in the literature of biosensing. In addition, note that we characterized the sensor for an analyte RI from 1.33 to 1.43; one of the reasons is that most of the biochemical and biomedical analytes vary within the RI range of 1.33–1.43 [12,13] . Moreover, we can see from Fig. 5(a) that the loss peak broadens for an analyte RI of 1.43 that leads to low AS of around 120 RIU$^{-1}$ [Fig. 5(b)]. Therefore, we characterize the sensor for an RI of up to 1.43, because further increase may lead to the false detection of analytes due to such broadening of the loss peak.

The proposed sensor shows that the full-width at half-maximum values are 130, 82, 71, 63, 55, 52, 47, 48, 59, and 138 for an analyte RI range of 1.33 to 1.42. With the

increase of the analyte RI, the resonance peak becomes sharper, however, after a certain RI loss spectra start broadening. Moreover, the linearity of the proposed sensor up to RI of 1.43 is $R^2 = 0.7789$; however, a more linear characteristic $R^2 = 0.9662$ is obtained up to RI of 1.42 [Fig. 5(c)]. In addition, the linearity between 1.42 and 1.43 is also shown in the inset Fig. 5(c), where the obtained $R^2$ is 0.9996.

Note that, due to low CL the sensor also attains a high sensor length in the range of cm that is suitable for practical sensing.

The sensor resolution and LOD are also two important factors in biosensing which control the extent to which the sensor can precisely detect small changes in sizes and the nearby RI [7,14] . Considering $\lambda_{min} = 0.1$ nm, according to WS, the maximum resolution of the sensor goes up to $9 \times 10^{-7}$ RIU. Therefore, the sensor can detect a tiny change of environmental RI variation that is of the order of $10^{-7}$. Moreover, based on the obtained maximum resolution, the maximum LOD of the sensor is $8.12 \times 10^{-12}$ RIU$^2$/nm which, to the best of our knowledge, is the best in the literature of biosensing.

In summary, we proposed a low loss, highly sensitive LSPR-PCF-based sensor for SERS response intensification in the visible to mid-IR spectrum. We demonstrated the way we obtained a sensor design with optimized geometrical parameters. This Letter shows that the sensor can attain, to the best of our knowledge, a record WS and AS of 111000 nm/RIU and 2050 RIU$^{-1}$ with maximum sensor resolution and LOD of $9 \times 10^{-7}$ RIU and $8.12 \times 10^{-12}$ RIU$^2$/nm, respectively. As shown in Fig. 1(b), the proposed sensor can be made using capillary stacking and can open new possibilities for highly sensitive and precise detection of bioanalytes.

## REFERENCES

1. S. A. Maier, P. G. Kik, H. A. Atwater, S. Meltzer, E. Harel, B. E. Koel, and A. A. Requicha, Nat. Mater. **2**, 229 (2003).
2. H. Wang, H. Zhang, J. Dong, S. Hu, W. Zhu, W. Qiu, H. Lu, J. Yu, H. Guan, S. Gao, Z. Li, W. Liu, M. He, J. Zhang, Z. Chen, and Y. Luo, Photonics Res. **6**, 485 (2018).
3. S. Cao, Y. Shao, Y. Wang, T. Wu, L. Zhang, Y. Hicsuang, F. Zhang, C. Liao, J. He, and Y. Wang, Opt. Express **26**, 3988 (2018).
4. A. A. Rifat, F. Haider, R. Ahmed, G. A. Mahdiraji, F. R. M. Adikan, and A. E. Miroshnichenko, Opt. Lett. **43**, 891 (2018).
5. J. Lu, Y. Li, Y. Han, Y. Liu, and J. Gao, Appl. Opt. **57**, 5268 (2018).
6. M. S. Islam, J. Sultana, A. A. Rifat, R. Ahmed, A. Dinovitser, B. W.-H. Ng, H. Ebendorff-Heidepriem, and D. Abbott, Opt. Express **26**, 30347 (2018).
7. D. Paul and R. Biswas, Opt. Laser Technol. **101**, 379 (2018).
8. J. R. DeVore, J. Opt. Soc. Am. **41**, 416 (1951).
9. A. Vial, A.-S. Grimault, D. Macías, D. Barchiesi, and M. L. de la Chapelle, Phys. Rev. B **71**, 085416 (2005).
10. B. Tatian, Appl. Opt. **23**, 4477 (1984).
11. A. A. Rifat, G. A. Mahdiraji, Y. M. Sua, R. Ahmed, Y. G. Shee, and F. R. Mahamd Adikan, Opt. Express **24**, 2485 (2016).
12. A. Aray, F. Chiavaioli, M. Arjmand, C. Trono, S. Tombelli, A. Giannetti, N. Cennamo, M. Soltanolkotabi, L. Zeni, and F. Baldini, J. Biophotonics **9**, 1077 (2016).
13. A. K. Yetisen, H. Butt, T. Mikulchyk, R. Ahmed, Y. Montelongo, M. Humar, N. Jiang, S. Martin, I. Naydenova, and S. H. Yun, Adv. Opt. Mater. **4**, 1589 (2016).
14. I. M. White and X. Fan, Opt. Express **16**, 1020 (2008).